Thermoelectric properties of chemically substituted full-Heusler $Fe_2TiSn_{1-x}Sb_x$ ($x = 0$, 0.1, and 0.2) compounds

Ilaria Pallecchi,[1,*] Marcella Pani,[1,2] Fabio Ricci,[3] Sébastien Lemal,[3] Daniel I. Bilc,[4] Philippe Ghosez,[3] Cristina Bernini,[1] Niccolò Ardoino,[2] Gianrico Lamura,[1] and Daniele Marré[1,5]

[1]*CNR-SPIN, Dipartimento di Fisica, Via Dodecaneso 33, 16146, Genova, Italy*

[2]*Dipartimento di Chimica e Chimica Industriale, Università di Genova, Via Dodecaneso 31, I-16146 Genova, Italy*

[3]*Physique Théorique des Matériaux, Q-MAT, CESAM, Université de Liège (B5), B-4000 Liège, Belgium*

[4]*Independent contribution, Str. Valea Girboului, RO-407280 Floresti, Romania*

[5]*Dipartimento di Fisica, Università di Genova, Via Dodecaneso 31, I-16146 Genova, Italy*

(Received 16 March 2018; revised manuscript received 6 June 2018; published 17 July 2018)

According to theoretical predictions [Phys. Rev. Lett. **114**, 136601 (2015)], Sb substitution in Fe_2TiSn full-Heusler compounds is thought to enhance the *n*-type thermoelectric power factors. We prepare Fe_2TiSn samples with 0%, 10%, and 20% Sb substitution on the Sn site and study the effects of the heat treatment protocol and of Sb substitution by structural characterization, electrical, thermoelectrical, and thermal transport measurements from room temperature down to 10 K, and by comparison with *ab initio* calculations. For the undoped Fe_2TiSn phase, we find a bad metallic gapless transport behavior in the as-cast sample and a small gap semiconducting behavior for the annealed samples. These observations, together with the *p*-type character emerging from the Hall effect and Seebeck effect, are explained by *ab initio* calculations, provided that antisite disorder and vacancy defects are included. In these undoped Fe_2TiSn samples, we find that increasing thermal annealing temperature up to 800 °C slightly decreases the carrier concentration, enhances the Seebeck coefficient in the low-temperature regime (below 100–200 K), induces magnetic ordering at low temperature (<150 K), and improves the thermoelectric figure of merit and power factor in the low-temperature regime (below ∼200 K). As for Sb substitution, we find that 10% substitution increases hole carrier concentration and induces a weakly metallic behavior as compared to the semiconducting behavior of the corresponding undoped annealed samples. On the other hand, 20% substitution lowers the carrier density and increases the resistivity by a factor ∼50, with semiconducting behavior measured in the whole temperature range. We interpret the observed effect of Sb doping as a complement to disorder. Indeed, using first-principles techniques we unearth the experimental signature related to density of states features induced by native impurities in the realized samples. The Seebeck coefficient exhibits a maximum at around 200–250 K for the undoped and 20%-doped samples, as typical of semiconducting compounds, while it increases monotonically with temperature for the metallic 10%-doped sample. The latter behavior, joined with the good electrical properties of the 10% sample, determines the room-temperature power factor of $\sim 1.3 \times 10^{-4}$ W K^{-2} m^{-1} in the 10% Sb-doped sample, more than twice as much as to the value of the undoped sample.

DOI: 10.1103/PhysRevMaterials.2.075403

I. INTRODUCTION

The recovery of waste heat, or at least a fraction of it, could significantly reduce overall energy consumption and prevent huge economic losses. Solid-state thermoelectrics enable direct and reversible conversion between heat and electricity and provide a promising solution for converting waste heat to electrical power. A measure of the conversion efficiency of thermoelectric material is its figure of merit ZT, defined as

$$ZT = \frac{S^2\sigma}{k}T,$$

where S, σ, T, and κ are respectively the Seebeck coefficient, the electrical conductivity, the absolute temperature, and the total thermal conductivity, the latter being composed of contributions from the lattice (κ_L) and the charge carriers (κ_e). As κ_e and σ are positively correlated in all known materials, the most effective way to reduce κ is to reduce κ_L. Indeed, one of the most pursued approaches in the research for new thermoelectrics is to use nanostructured features to tune electrical and thermal transport, quasi-independently, in such a way that irreversible heat transport is minimized while simultaneously maintaining good electrical properties. Three general strategies to reduce the lattice thermal conductivity are as follows: (i) induce phonon scattering within the unit cell by creating rattling structures or point defects such as interstitials, vacancies, or by alloying; (ii) use complex crystal structures to separate the electron crystal from the phonon glass, i.e., achieve a phonon glass without disrupting the crystallinity of the electron-transport region; and (iii) scatter phonons at interfaces in multiphase composites mixed at the nanometer scale, such as thin-film superlattices, intimately mixed composite structures, and randomly stacked nanocrystals. Theoretical prediction for lower limits of thermal conductivity in materials can be by far overcome via nanostructuring [1]. In general, minimization of

*Corresponding author: ilaria.pallecchi@spin.cnr.it

lattice thermal conductivity can be obtained by introducing defects of different dimensionality to limit the mean free path of phonons of different wavelengths in systems with weak chemical bonds and/or heavy atomic masses, which are associated to reduced group velocity of acoustic phonons, in systems with complex crystal structures and/or large primitive cells, where the relative contribution of acoustic phonons to heat transport is reduced [2]. On the other hand, maintaining good electrical properties requires maximizing the power factor $PF = S^2\sigma$, which is generally achieved by targeting a high carrier mobility, as well as by selecting materials with favorable electronic structure. Indeed, in the direction of material screening, optimal thermoelectric properties are searched in crystalline materials (possibly exploring chemical substitutions in known thermoelectric materials) with unique structure-property relationships that yield the desired combination of properties to maximize PF and ZT. Multiple strategies, when combined in a single system, can lead to enhanced thermoelectric performance. This is called a panoscopic [3,4] approach and it includes the following:

(i) all-scale hierarchical architecturing,
(ii) matrix/inclusion band alignment engineering, and
(iii) intramatrix electronic structure engineering.

Clearly other material requirements are important for applications, such as thermal stability, mechanical strength at high temperatures, and composition with abundant, cheap, and nontoxic elements.

Among promising thermoelectric materials, Skutterudites [5], clathrates [6], half-Heusler [7,8], and full-Heusler [9] compounds represent efficient examples of the phonon-glass electron-crystal concept first introduced by Slack [10]. In these compounds, guest atoms introduced into the voids of an open cage structure, the so-called "phonon rattlers," act as phonon-scattering centers and interact with a broad spectrum of phonons, thus reducing the phonon thermal conductivity. At the same time, electronic properties are determined mainly by the cage structure framework, i.e., the electron-crystal, and are preserved upon introduction of disorder into the cage voids. Moreover, the complex crystal structure and stoichiometry of Skutterudites, clathrates, half-Heusler, and full-Heusler compounds offers multiple opportunities not only of creating rattling structures and point defects such as interstitials, vacancies, and disorder due to alloying, but also of engineering the electron [11] and phonon [12,13] band structure.

Full-Heusler compounds [9] have a general formula X_2YZ, where X, Y, and Z represent a combination of a large variety of elements (X = Mn, Fe, Co, Ni, Cu, Ru, Rh, Pd, Ag, Cd, Ir, Pt, Au; Y = Li, Be, Sc, Ti, Cr, Mn, Fe, Co, Ni, Y, Zr, Nb, Mo, Hf, W, rare earth; Z = B, Al, Si, Zn, Ga, Ge, As, In, Sn, Sb, Pb, Bi). Heusler phases are stable up to high temperatures and are generally composed of abundant, cheap, and nontoxic elements. They often display considerable amounts of atomic disorder, specifically, a natural tendency toward off-stoichiometry, predictable from thermodynamic theory, which creates natural (intrinsic) doping via vacancies, antisites, or swaps [14–17], and may affect transport properties, as observed experimentally in full-Heusler Fe_2TiSn [16], and predicted even more dramatically in ferromagnetic full-Heusler compounds [15]. Their crystal structure is composed by four interpenetrating fcc lattices. From the electrical point of view, they are half-metallic and their properties depend more on the valence count than on constituent elements. The thermoelectric behavior has been mostly studied in half-Heusler compounds, as they have narrow bands, associated to high effective masses, which yields large Seebeck coefficients. Half-Heusler compounds exhibit a Seebeck coefficient S up to $\sim 300\,\mu V/K$ at room temperature and high electrical conductivity ($\sim$1000–10000 $\Omega^{-1}\,cm^{-1}$) [18–22]. Their relatively high thermal conductivity (as high as $10\,W m^{-1}\,K^{-1}$) must be reduced. Lattice thermal conductivity has been reduced and ZT enhanced in these compounds by nanostructuring, introduction of electrically nonactive nanocomposites, phase separation, deposition of thin films and multilayers, and isoelectronic alloying, which enhances the phonon scattering by point defects due to mass differences (mass fluctuations) and size differences (strain field impurities) between the impurity atoms and the host atoms, without introducing charge disorder [9]. Moreover, it is possible to dope each of the occupied fcc sublattices individually in order to optimize thermoelectric properties. For example, it is possible to alter the number of charge carriers by doping on the Z position, and simultaneously introduce disorder by doping on the X and Y position, resulting in mass fluctuations, which can decrease the lattice thermal conductivity κ_L. Within the half-Heusler family, TiNiSn-based compounds are promising as n-type thermoelectrics and TiCoSb- and FeRSb-based (R = V, Nb, Ti) compounds as p-type thermoelectrics. Noteworthy, ZrNiSn can be converted from n-type to p-type by addition of Co and Ir; these p-type and n-type materials are thermoelectrically compatible and have similar thermal expansion coefficients, they are industrially processable and made of available and low-cost elements, and moreover they have good mechanical properties and thermal stability; hence they are remarkable candidates for thermoelectric modules. Record values of thermoelectric figure of merit ZT have been obtained in n-type $Ti_{0.5}Zr_{0.25}Hf_{0.25}NiSn_{0.998}Sb_{0.002}$ (ZT = 1.5 at 700 K [23], ZT = 1.2 at 830 K [24]) and in p-type $FeTi_{0.2}Nb_{0.8}Sb$ (ZT = 1.1 at 1100 K [25]). In full-Heusler systems, lower figure-of-merit values ZT = 0.1–0.2 have been obtained [26–28], but remarkable power factors $PF \approx 6.5\,mW/mK^2$ at 340 K in $Fe_2V_{1+x}Al_{1-x}$(x = 0.05) [28] and $PF \approx 0.4\,mW/mK^2$ at room temperature in $Fe_{2-x}Mn_xTiSn$(x = 0.0185) [29] suggest that a significant edge of improvement could exist if the thermal conductivity is decreased and PF is further increased via manipulation of electronic properties, e.g., via doping. Hole-type doping in Fe_2TiSn has been explored by Mn substitution on the Fe site in samples prepared by arc melting plus spark plasma sintering (SPS) [29], and a more than double increase in the PF at room temperature has been measured in the doped samples as compared to the undoped one, which has been attributed to enhanced density of states close to the Fermi level. Fe_2VAl can be doped n-type or p-type both on the V [28,30,31] and on the Al [28,32] site, and power factors in the range 5–9 mW/mK^2 above room temperature have been obtained by doping.

A recent theoretical work [11] has verified that, to enhance PF, good thermoelectric materials should combine (i) a distribution of carrier energy as narrow as possible and (ii) high carrier velocities in the direction of the applied field [33]. Satisfying both of these criteria seems difficult in practice, as narrow energy distributions are typically

associated with flat energy bands while high carrier velocities are necessarily associated with highly dispersive bands. *Ab initio* calculations on Fe_2YZ full-Heusler compounds with Y = Ti, Zr, Hf and Z = Si, Ge, Sn have suggested that by engineering the appearance of flat-and-dispersive Fe e_g states at the bottom of the conduction bands, originating from highly directional orbitals, n-type power factors 4–5 times larger than in classical thermoelectrics (such as PbTe or Bi_2Te_3) can be obtained within a rigid-band approach at room temperature [11]. Another theoretical work has predicted that, thanks to such flat bands as close as 0.04 eV to the Fermi level [16], carrier doping in the range 10^{20}–10^{21} cm^{-3} in full-Heusler Fe_2TiSn may yield enhanced thermoelectric properties and ZT values as large as 0.6 at room temperature [34], consistently with the predictions of Ref. [11]. In the present work, the exploitation of the Fe e_g "flat-and-dispersive" band, located at the bottom of the conduction band, is witnessed by explicitly substituting part of the Sn atoms by Sb. This procedure, on one side, furnishes charge carriers to the system, shifting the Fermi level close to this band and, on the other side, does not perturb it, keeping thus the rigid-band picture valid. Our goal is exploring the predicted increment of the power factor from a combined experimental and theoretical approach. We prepare Fe_2TiSn full-Heusler samples with 0%, 10%, and 20% Sb substitution on the Sn site via an arc-melting route and postannealing. After optimization of the heat treatment protocol, carried out by characterization of structural as well as electrical and thermoelectrical properties of undoped samples, we explore the effect of Sb substitution on electrical and thermoelectrical properties from room temperature down to low temperature. We interpret our data with *ab initio* calculations of electronic band structure, demonstrating the crucial role of antisite defects and atomic vacancies on the transport properties of real samples. Despite the detrimental role of such atomic disorder, which is not addressed in Ref. [11], responsible for p-type power factors at room temperature $\sim 10^{-4}$ W K^{-2} m^{-1}, 2 orders of magnitude smaller than the n-type values predicted in ideal $Fe_2TiSn_{1-x}Sb_x$, we obtain a twofold improvement of the room-temperature power factor in the 10% Sb-doped sample as compared to the undoped sample.

II. METHODS

Polycrystalline samples of Fe_2TiSn, $Fe_2TiSn_{0.9}Sb_{0.1}$, and $Fe_2TiSn_{0.8}Sb_{0.2}$ are prepared starting from pure elements (99.9 wt% purity for Fe and Sn, 99.99 wt% purity Ti, and 99.999 wt% Sb) weighed in stoichiometric quantities. The metals, in small pieces, are first pressed together to form a pellet and then arc melted in a high-purity argon atmosphere, after the fusion of a Ti-Zr alloy as a getter. The buttons are remelted several times after turning them upside-down, in order to ensure a good homogenization. After melting, the samples are wrapped in Ta foils, closed in silica ampoules under vacuum, and annealed. The annealing conditions are chosen after some preliminary tests on the undoped compound, treated at temperatures between 600 °C and 800 °C for a time varying between 7 and 30 days. A thermal treatment at 700 °C for 8 days is then applied to all samples as a compromise between results in terms of phase purity and homogeneity and an overly long annealing time.

Both as-cast and annealed samples are characterized by x-ray powder diffraction and microscopic techniques. X-ray diffraction analysis is carried out by means of a powder diffractometer in reflection mode (Bragg-Brentano geometry, Ni-filtered $Cu\,K\alpha$ or Fe-filtered $Co\,K\alpha$ radiations, silicon as an internal standard, $a = 5.4308$ Å). Intensity data for Rietveld refinements are collected in 10–110° 2ϑ range, with 0.02° in ϑ steps and counting times of 15–20 s/step. The structural fits are done by means of the FULLPROF program [35]. The homogeneity of the samples is checked by a scanning electron microscope–energy dispersive system (EDS) (Leica Cambridge S360, Oxford X-Max20 spectrometer, with software Aztec). After standard micrographic preparation, the specimens are graphitized and analyzed at a working distance of 25 mm, with acceleration voltage 20 kV.

Magnetic susceptibility χ(T) is measured in a commercial superconducting quantum interference device (SQUID) magnetometer by Quantum Design from 1.8 to 300 K in magnetic fields 50–100 Oe. Electrical resistivity (ρ), magnetoresistivity, and Hall resistance (R_H) measurements by four-probe technique are performed in a physical properties measurement system (PPMS) by Quantum Design at temperatures from room temperatures down to 10 K and in magnetic fields up to 90 000 Oe. The Seebeck (S) effect and thermal conductivity (κ) are measured with the PPMS thermal transport option in continuous scanning mode with a 0.4 K/min cooling rate.

III. COMPUTATIONAL DETAILS

Density functional theory (DFT) [36] calculations are performed using the CRYSTAL code [37,38] within the B1 Wu-Cohen [39] (B1-WC) hybrid functional. The full-electron basis sets are taken from Ref. [40] for Fe, Ref. [41] for Ti, and Ref. [42] for Sn. A $9 \times 9 \times 9$ Monkhorst-Pack grid of k points in the irreducible Brillouin zone is used to ensure a total energy convergence of about 0.01 meV and is used to perform the relaxation of the pristine structure. An $18 \times 18 \times 18$ mesh is used to refine the electronic structure after relaxation. The energy convergence criterion has been fixed to 10^{-9} Ha for the self-consistent field calculations. For geometry relaxation of the pristine phase, we fix a threshold of 3×10^{-4} Ha/Bohr on the root-mean-square values of energy gradients and of 1.2×10^{-3} Bohr on the root-mean square values of atomic displacements. A Gaussian smearing of the Fermi surface is set to 3.2×10^{-4} Ha. For transport properties, we use the BOLTZTRAP [43] code, which performs calculations of the transport and thermoelectric tensors within the Boltzmann semiclassical approach and in the constant relaxation time approximation (CRTA), exploiting the eigenenergies as calculated from DFT (with a denser k-space sampling of $53 \times 53 \times 53$). The thermoelectric properties of doped Fe_2TiSn are calculated considering a shift of the chemical potential μ with respect to electronic states in a rigid-band approximation. Within the CRTA, the scattering mechanisms are purposely ignored and the Seebeck and Hall coefficients do not depend anymore on the relaxation time. Possible native point defects are also studied in a $2a \times 2a \times 2a$ ($a = 5.912$ Å) cubic supercell (128 atoms) containing one defect (with density of about 6×10^{20} cm^{-3}). Ti and Sn neutral vacancies (referred to as V_{Sn} and V_{Ti} in the text) are modeled by means of the ghost atoms, i.e., the

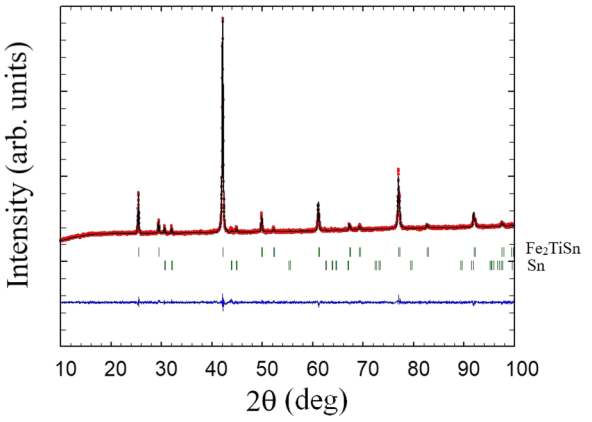

FIG. 1. Rietveld refinement plot of the as-cast Fe_2TiSn sample. Red, black, and blue lines correspond to experimental, calculated, and difference (observed minus calculated) curves, respectively. Vertical bars represent Bragg positions of reflection peaks. The sample contains elemental Sn as secondary phase (4 wt %). $R_B = 2.31$ (main phase Fe_2TiSn), $R_{wp} = 2.03$, $\chi^2 = 1.53$.

associated cores and electrons are removed from the cell but the basis set associated to the original atom remains on the site to properly model the electron density within the vacancy [38]. Regarding the antisite defects, we build two systems by switching the position of nearest-neighbors Ti-Fe (Ti_{Fe}) and Sn-Fe (Sn_{Fe}). The electronic structure of the supercells is estimated at the fixed pristine geometry (a) using a $5 \times 5 \times 5\,k$ grid, since the geometrical relaxation of the atoms surrounding the defect is not expected to change the donor/acceptor nature of these defects.

IV. EXPERIMENTAL RESULTS

A. Undoped Fe_2TiSn samples annealed at different temperatures

The results of both x-ray diffraction and microscopy evidence that the Fe_2TiSn phase with Heusler's $L2_1$-type structure (cF16, Fm-$3m$, prototype: $MnCu_2Al$) forms already in the as-cast sample, in agreement with the thermodynamical stability predicted by theory [11] and with known data on ternary Ti-Fe-Sn phases available in the literature [44]. The x-ray pattern of the as-cast sample is shown in Fig. 1. The EDS analyses show a compositional variability within ∼1 at % in the undoped sample, with Fe slightly in excess and Ti slightly in defect with respect to the ideal stoichiometry 2:1:1. Moreover, the formation of the Fe_2TiSn phase is always accompanied by the presence of one or more extra phases in small percentages (<5 wt %), which are typically Sn and/or Ti finely dispersed in the matrix, but also binary or ternary compounds. In particular, the as-cast sample contains traces of Sn (see Fig. 1) and Ti. The sample annealed at 600 °C contains traces of FeSn and Sn, while in the sample annealed at 800 °C, the two ternary phases $(Fe,Ti)Sn_2$ and $Fe_2(Ti,Sn)$ appear in addition to small traces of Sn and Ti. Among all samples, the one annealed at 700 °C proved to be the most homogeneous, with only the presence of Sn as an extra phase; consequently, 700 °C is chosen for the thermal treatment also of the Sb-doped samples. Yet we find that the heat treatment is mostly effective in reducing the

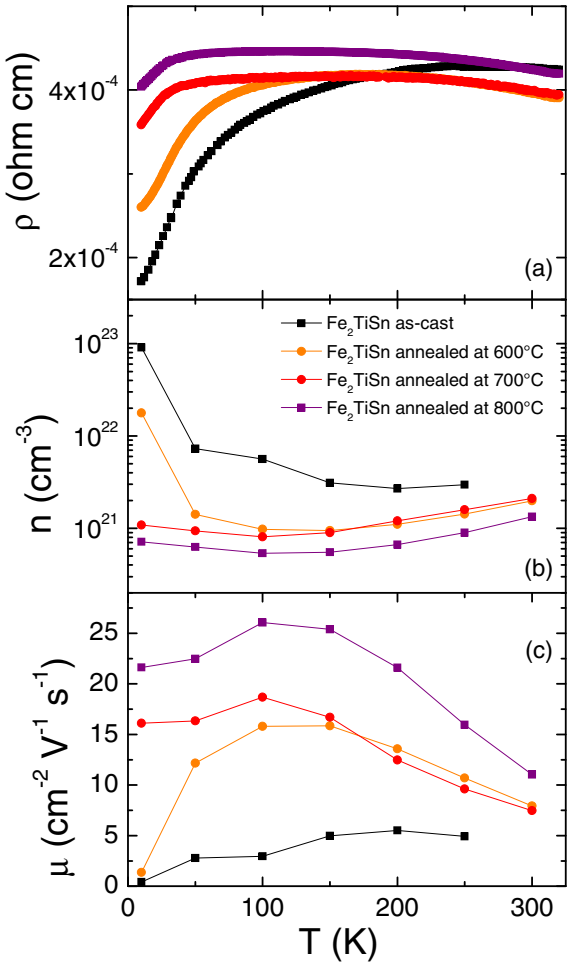

FIG. 2. (a) Resistivity curves of Fe_2TiSn prepared with different heat treatments. (b) Carrier density curves of the same samples extracted from Hall effect measurements. (c) carrier mobility curves of the same samples.

stresses and strains caused by the rapid cooling of the sample after the arc-melting process, while it has only a minor effect in improving the sample monophasicity. Detailed structural analysis will be published elsewhere [45].

In Fig. 2, we present resistivity, carrier density, and mobility curves measured in undoped samples obtained by different thermal treatments, namely, as cast and annealed at 600 °C, 700 °C, and 800 °C for several days. In all cases, two or three pieces of the prepared lump are measured and compared, as a test of homogeneity. The absolute values are affected by a significant uncertainty (∼20%) related to the estimation of the geometrical factors due to the irregular shape of the pieces. However, the temperature dependence evidences the transport mechanisms come into play. In Fig. 2(a), the resistivity ρ curves exhibit either a gapless bad metallic behavior with positive temperature derivative $d\rho/dT$ above 100 K (as-cast sample) or a small gap semiconducting behavior with negative temperature derivative $d\rho/dT$ above 100 K (annealed samples). In all cases the temperature dependence is very weak, in contrast with the larger negative temperature derivative $d\rho/dT$ that could be expected from the ideal Fe_2TiSn compound with ∼1-eV band gap in the calculated electronic structure [11,34]. In Ref. [16],

the small gap semiconducting behavior is ascribed to Fe-Ti antisite disorder. The shapes of the curves are consistent with literature data on either Fe-deficient samples (compare the Fe-deficient sample $Fe_{1.9}TiSn$ in Ref. [46]) or samples with excess Fe and deficient Ti stoichiometry (compare the Fe-Ti off-stoichiometric samples $Fe_{2.05}Ti_{0.95}Sn$ in Refs. [47,48]). This literature comparison suggests that an exact determination of stoichiometry is extremely difficult; however, our energy dispersive x-ray (EDX) analyses indicate ∼1 at % Fe excess and ∼1 at % Ti deficiency, in agreement with Ref. [47]. In Fig. 2(b), the carrier concentrations extracted from the Hall effect measurement in a single band picture are plotted as a function of temperature. The temperature dependence is weak. The carrier density increases below 50 K with decreasing temperature, more visibly for the as-cast and 600 °C annealed samples. This crossover at 50 K is the counterpart of the crossover observed in the resistivity curves, more evident for the as-cast and 600 °C annealed samples. In the temperature regime above 50 K, the carrier density values are all around 10^{21} cm^{-3}. It is seen that with increasing annealing temperature the carrier density slightly decreases. The positive sign of the Hall signal points to hole-type carriers. In Fig. 2(c), the carrier mobilities are extracted from the inverse product of resistivity and carrier concentration. Values in the range of a few to tens of $cm^2\,V^{-1}\,s^{-1}$ are obtained, and a trend of increasing mobility with increasing annealing temperature is seen, possibly suggesting that annealing heals microstructural or substitutional disorder. Following Ref. [49], we estimate the degree of atomic disorder from the relative height of x-ray diffraction peaks: the ratio of (111) to (220) peak intensities is used as a measure of Ti-Sn antisite disorder and Ti or Sn vacancies, while the ratio of the (200) to (220) peak intensities is used as a measure of disorder in the Fe site. We find that both ratios I_{111}/I_{220} and I_{200}/I_{220} increase monotonically and almost double with increasing annealing temperature up to 800 °C. Hence, x-ray data confirm the result from carrier mobility that annealing heals atomic disorder.

In Fig. 3, we present magnetoresistivity $(\rho(H)\text{-}\rho(0))/\rho(0)$ curves measured at selected temperatures for the as-cast sample and for the sample annealed at 700 °C, the latter being representative of the magnetoresistivity behavior of all the annealed samples. Whereas for the as-cast sample an almost vanishing magnetoresistivity lower than 0.6% at 90 000 Oe is observed, in the annealed samples a sizeable negative contribution is observed at low temperature. While below 50 K the cusplike shape of the magnetoresistivity curves is suggestive of a weak localization mechanism, at intermediate temperatures of 100–150 K the negative few percent magnetoresistivity may be of magnetic origin.

In Fig. 4 we present the Seebeck coefficient S, thermal conductivity κ, thermoelectric figure of merit ZT, and power factor $S^2\sigma$ curves as a function of temperature. The Seebeck curves in Fig. 4(a) are positive for all samples, indicating that thermoelectric transport is dominated by hole carriers. S values are in the range of 10–20 μV/K at room temperature. The S curve of the as-cast sample increases monotonically, almost linearly, with increasing temperature, as expected from a metal with constant carrier density, while the S curves of the annealed samples exhibit a broad maximum at around 200–250 K, which tends to shift to higher temperatures with increasing

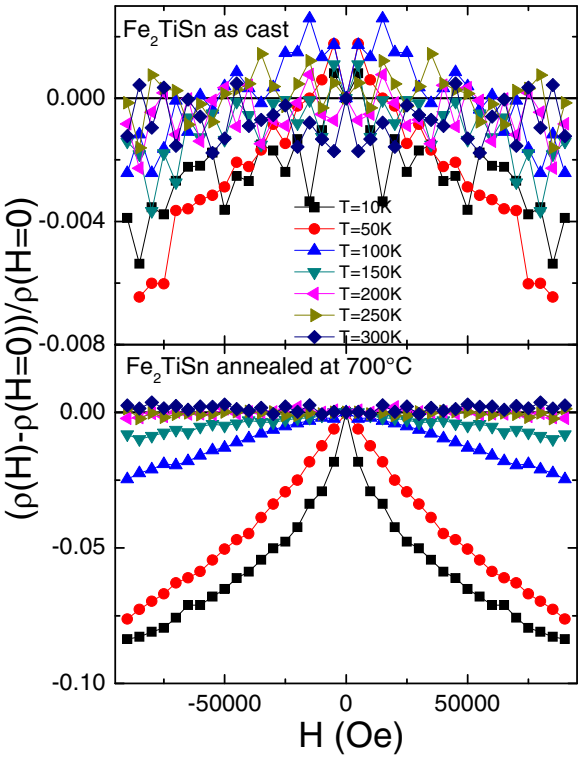

FIG. 3. Magnetoresistivity curves of Fe_2TiSn as-cast (upper panel) and annealed (lower panel) samples.

annealing temperature. Seebeck curves of such shapes are typical of semiconducting samples. These behaviors suggest that the hole carriers have a degenerate or metallic character in the case of the as-cast sample and a thermally activated character for the annealed samples, consistent with the resistivity curves shown in Fig. 2(a). The thermal conductivity curves shown in Fig. 4(b) are characterized by a maximum slightly below 100 K, which marks the crossover between the low-temperature regime, where κ increases with temperature due to increasing excitation of phonon modes, and the high-temperature regime, where phonon-phonon scattering counterbalances the further activation of phonon modes. The sharpness of the peak demonstrates the good structural quality of the samples, as such a peak would be easily washed out by any type of disorder that is effective in limiting the phonon mean free path. The room-temperature values of the thermal conductivity are pretty low, in the range of few $W\,K^{-1}\,m^{-1}$. In Fig. 4(c), the figure-of-merit ZT curves are plotted. Values in the range 10^{-3}–10^{-2} are reached at room temperature. Interestingly, mainly as a result of the S temperature dependence, the ZT curve of the as-cast sample is smaller in the temperature range below 200 K but monotonically increases with temperature up to room temperature, whereas for the annealed samples the ZT curves exhibit a maximum below room temperature. The behavior of S curves is also reflected in the power factor curves, shown in Fig. 4(d). Also, in this case the $S^2\sigma$ curve of the as-cast sample monotonically increases with temperature up to room temperature, while the curves of the annealed samples exhibit a maximum below room temperature. Noteworthy, the sample annealed at 800 °C has the largest power factor of $\sim 10^{-4}\,W\,K^{-2}\,m^{-1}$, around 200–250 K. This value

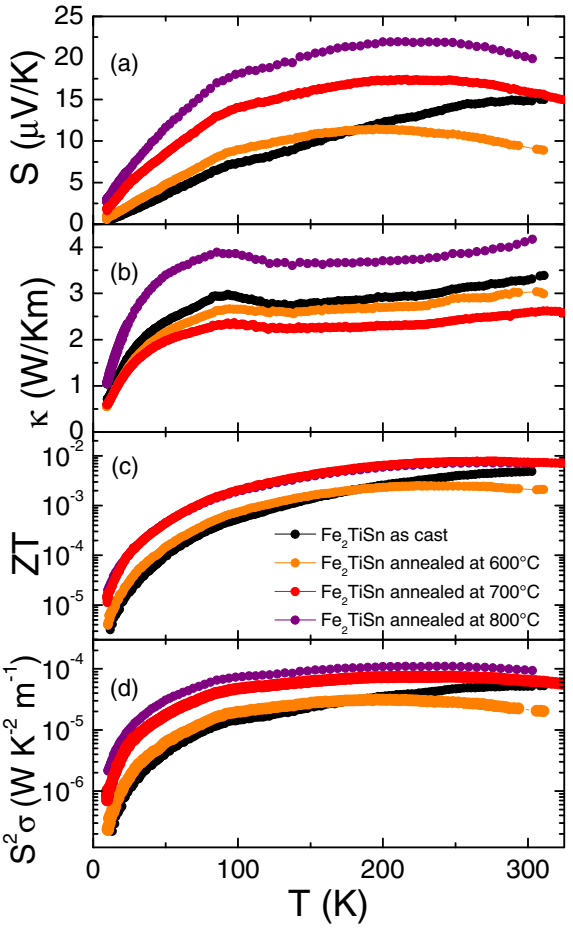

FIG. 4. (a) Seebeck coefficient curves of Fe_2TiSn samples prepared with different heat treatments, (b) thermal conductivity curves, (c) thermoelectric figure of merit, and (d) power factor curves.

is slightly smaller than $\sim 1.5 \times 10^{-4}$ W K^{-2} m^{-1} at 300 K recently obtained in undoped Fe_2TiSn samples, sintered by spark plasma sintering under a pressure of 50 MPa at 800 °C K for 5 min [29].

In Fig. 5, the low-field (50–100 Oe) magnetic susceptibility $\chi(T)$ curves of the as-cast and annealed Fe_2TiSn samples are displayed. For the as-cast sample, the magnetic signal is 10 times smaller than for the annealed samples, thereby for clarity it is magnified and plotted separately on the right-hand axis. The small magnitude of the as-cast magnetic signal is consistent with the absence of any magnetic contribution in magnetoresistivity (see the absence of negative contribution in Fig. 3). A ferromagnetic ordering appears below 260 K, and it is well visible in the as-cast sample but also present in the annealed samples (not visible in the scale of Fig. 5). The $\chi(T)$ curve of the as-cast sample is in agreement with literature reports [50,51]. In the annealed samples, a further ferromagnetic ordering develops below 50 K which could be associated with the regime crossover observed in resistivity and carrier density curves at the same temperature (see Fig. 2). The presence of such magnetic contribution in both magnetotransport and susceptibility measurements suggests that it may be a characteristic of the main phase rather than related to secondary phases.

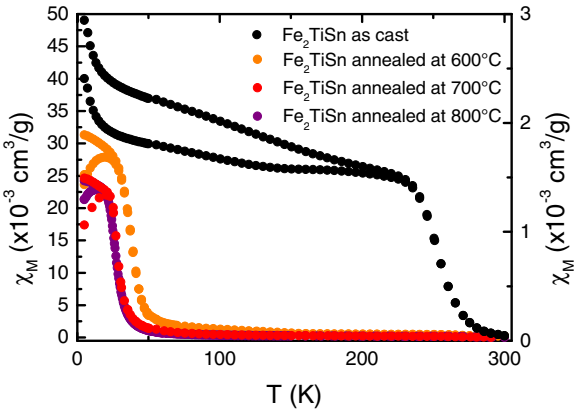

FIG. 5. Zero-field-cooled and field-cooled magnetic susceptibility $\chi(T)$ curves of Fe_2TiSn samples prepared with different heat treatments. For the as-cast sample, the magnetic signal is 10 times magnified and plotted separately on the right-hand axis.

In summary, after consideration of uncertainty regarding geometrical factors, we can gather that with increasing annealing temperature:

(i) the carrier concentration slightly decreases;

(ii) the mobility slightly increases;

(iii) the Seebeck coefficient is larger in the low-temperature regime (below 100–200 K);

(iv) a magnetic contribution appears at low temperature; and

(v) as a result of electric and thermoelectric properties, ZT and power factor increase in the low-temperature regime (below ~200 K).

We note that due to the linear increase of its $S(T)$ curve, the as-cast sample has a room-temperature ZT value comparable to those of the annealed samples.

B. Sb-doped Fe_2TiSn samples

In view of preparing $Fe_2TiSn_{1-x}Sb_x$ samples, we should start from an undoped sample whose properties are as close as possible to theoretical predictions [11]. In order to maximize the beneficial effect of Sb doping on thermoelectric properties, the ideal undoped Fe_2TiSn compound to start from should have a carrier concentration as low as possible and exhibit no atomic site disorder and magnetic ordering. All our undoped samples exhibit higher carrier concentrations of $\sim 10^{21}$ cm^{-3}, and magnetic behavior below 50 K is observed in annealed samples. Moreover, the weak temperature dependence of resistivity and p-type character of charge carriers of all undoped samples are inconsistent with the ~1-eV band-gap electronic structure predicted by theory [11]. Before clarifying the origin of such anomalous properties of real undoped samples by simulating atomic defects in *ab initio* calculations, we explore the effect of Sb doping. We consider the following points: (i) annealed samples have a lower carrier concentration [see Fig. 2(b)] and we assume that the lower carrier concentration is a primary requirement to emphasize the effect of Sb doping; (ii) annealed samples have higher S, higher ZT, and higher power factors (see Fig. 4); (iii) it is plausible that with doping the semiconductinglike shape of the $S(T)$ curve of annealed

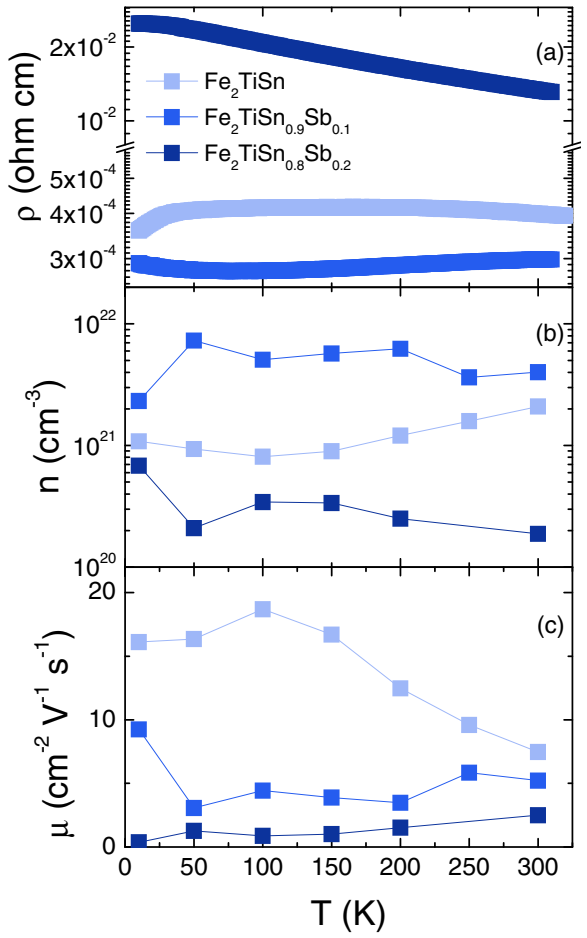

FIG. 6. (a) Resistivity curves of $Fe_2TiSn_{1-x}Sb_x$ ($x = 0.0$, 0.1, and 0.2) annealed at 700 °C, (b) carrier density curves of the same samples extracted from Hall effect measurements, and (c) carrier mobility curves of the same samples.

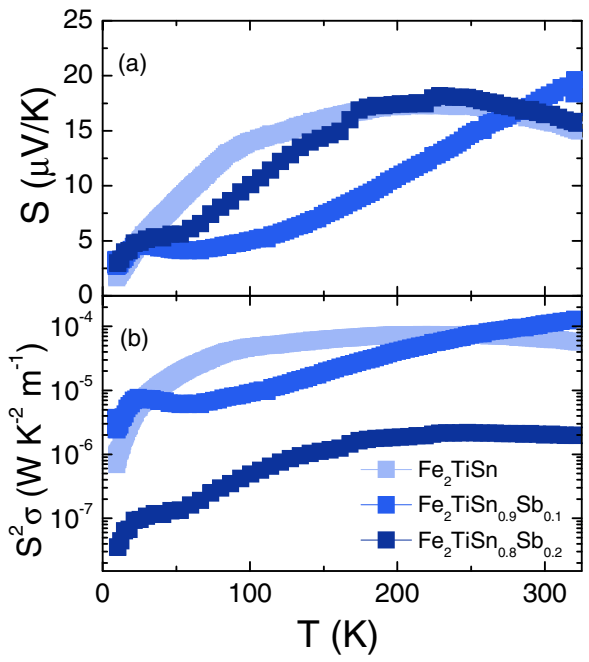

FIG. 7. (a) Seebeck coefficient curves of $Fe_2TiSn_{1-x}Sb_x$ ($x = 0.0$, 0.1, and 0.2) annealed at 700 °C and (b) power factor curves.

samples with a maximum at 200–250 K [see Fig. 4(a)] is turned into a metallicke, monotonically increasing $S(T)$ curve shape, thus improving thermoelectric properties at room temperature and above, which is the most interesting temperature range for applications; and (iv) in samples annealed at 700 °C, higher phase purity is detected in the SEM-EDS analyses as compared to those annealed at 800 °C. After these premises, we choose to prepare Sb-doped samples following the temperature annealing protocol at 700 °C for 8 days.

Figure 6 shows the electronic transport properties of undoped Fe_2TiSn and Sb-doped samples $Fe_2TiSn_{1-x}Sb_x$ $x = 0.1$ and 0.2 annealed at 700 °C. In Fig. 6(a), it is seen that with respect to the bad-metal behavior of the undoped sample exhibiting very weak temperature dependence, 10% Sb doping decreases the resistivity and induces a mild metallic behavior while 20% doping increases the resistivity by a factor of ∼50 and induces a semiconducting behavior in the whole temperature range. Consistently, in Fig. 6(b), it is seen that the hole carrier concentration increases by almost an order of magnitude from the undoped to the 10% doped sample, while in the 20% doped it decreases back below the value of the undoped sample. It must be noted that Sb doping is expected to introduce electron-type charge carriers in the ideal Fe_2TiSn structure; hence the increase in hole carrier concentration with 10% Sb doping is unexpected and any data interpretation should take into account the disordered nature of real undoped samples on which Sb doping is explored. This is done in the next section. We mention that the effect of Sb doping up to 5 at % on Fe_2TiSn resistivity was studied in the temperature range 300–850 K, but a negligible effect was found [16]. We also mention that the fully substituted Fe_2TiSb compound is predicted to be a half metal with 100% spin polarization [52]. Finally, in Fig. 6(c), the mobility decreases monotonically with increasing doping.

The magnetoresistance of 10% and 20% doped samples (not shown) exhibit negative contributions of a few percent in magnitude, very similar in shape as those found in all annealed undoped samples (see lower panel of Fig. 3), indicative of magnetic ordering. In Fig. 7, thermoelectric properties of the same undoped and Sb-doped samples $Fe_2TiSn_{1-x}Sb_x$ are displayed. In the top panel, with respect to the Seebeck curve of the undoped sample, exhibiting a broad maximum at 200–250 K, 10% doping induces a monotonic increase of S with temperature, as expected from metals with nearly constant charge-carrier density. The room-temperature value of the 10% doped sample exceeds that of the undoped sample. On the other hand, 20% doping results in an S curve shape similar to the undoped sample, consistent with the semiconducting behavior shown in the upper panel of Fig. 6. In the bottom panel of Fig. 7, the power factor $S^2\sigma$ curves are displayed. It is seen that 10% doping yields a $S^2\sigma$ curve that increases with increasing temperature above 60 K, yielding a crossover of the $S^2\sigma$ curves of the undoped and 10% doped samples at room temperature. The $S^2\sigma$ value of the 10% doped sample slightly above room temperature is more than twice the $S^2\sigma$ value of the undoped sample. On the contrary, 20% doping

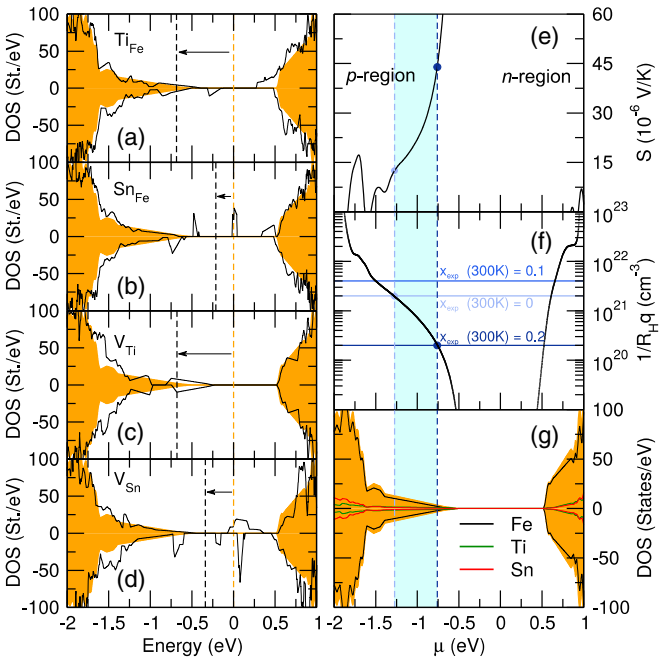

FIG. 8. Theoretical results from DFT and Boltzmann transport theory calculations. On the left column, the electronic DOS is shown, computed for a $2a \times 2a \times 2a$ cubic supercell of Fe_2TiSn containing one (a) Ti_{Fe}, (b) Sn_{Fe}, (c) V_{Ti}, and (d) V_{Sn} defect. The orange background refers to the pristine DOS, and the vertical dashed lines indicate the Fermi level associated with each DOS, with arrows highlighting their shift caused by the impurity. On the right column, we show the (e) chemical potential dependence of the Seebeck coefficient at 300 K, (f) the associated carrier density estimated by the inverse Hall coefficient (with the hole density identified from Hall measurements for $x = 0$, 0.1, and 0.2, highlighted within horizontal lines), and (g) the computed pristine atomic-projected DOS. The experimental carrier densities at 300 K for $x = 0$ and $x = 0.2$ are used to define a chemical potential interval (light blue region) falling inside the valence band.

suppresses the power factor severely by 2 orders of magnitude. Again, we mention that lower Sb substitution ($\leqslant 5\%$) results in minor effects on high-temperature thermoelectric properties, according to Ref. [16]. As for the thermal conductivity data, from the Wiedmann-Franz law it comes out that the thermal conductivity is dominated by the phonon contribution in the whole temperature range for all the samples. It is expected that doping suppresses thermal conductivity, as a consequence of mass fluctuations or strain field fluctuations [53,54]. Yet, our data, not shown here, do not allow any clear conclusion on the effect of doping on the thermal conductivity. Indeed, we observe a nonmonotonic behavior of thermal conductivity with doping, whose explanation is not clear.

V. THEORETICAL RESULTS

Pristine Fe_2TiSn is found to be a nonmagnetic semiconductor with a band gap of 1.04 eV [as shown in Figs. 8(a)–8(d) and 8(g) with orange background]. This is in agreement with the Slater-Pauling rule [55,56] but contrasts with the measured high hole density and the low Seebeck coefficient of the undoped samples [see Figs. 2(b) and 4(a)]. Similar discrepancies have been already found and explored in Fe_2VAl, for which it has been argued that the measured semimetallic character arises from antisite defects and disorder rather than being an intrinsic property of the pristine phase [57]. In order to investigate and clarify the differences between experiments and simulations occurring in Fe_2TiSn, we estimate the influence on electronic properties of such native defects as antisites and vacancies, whose presence is evidenced in the undoped samples by our structural analyses. The simulated electronic density of states (DOS), calculated for a $2a \times 2a \times 2a$ cubic supercell with one (a) Ti_{Fe}, (b) Sn_{Fe}, (c) V_{Ti}, and (d) V_{Sn} defect, are shown in Fig. 8. From here, we see that (i) all the defects act as acceptor dopants, shifting the Fermi level toward the valence band; (ii) in-gap states appear with respect to the pristine phase; and (iii) the spin degeneracy is removed. These results suggest that the as-cast undoped Fe_2TiSn samples are p-type doped due to the formation of defects and they consistently justify the bad-metal behavior of the resistivity (Fig. 2), the possible magnetic ordering appearing at low temperature (Figs. 3 and 5), and the holelike transport (Figs. 2 and 4). In Figs. 8(e) and 8(f), we show the room-temperature Seebeck coefficient and the carrier density as a function of the chemical potential μ for the pristine Fe_2TiSn phase. Following the rigid-band approach, i.e., due to the presence of acceptor defects, μ rigidly shifts toward the valence band, we recognize that the experimental hole density measured by the Hall effect at 300 K, $n_{300\,K} \approx 2 \times 10^{21}\,cm^{-3}$, identifies μ inside the valence band [see Fig. 8(f)], for which the corresponding calculated S is 12 μV/K, in good agreement with the measurements shown in Fig. 4. Upon Sb substitution on Sn sites, providing additional electrons to the system, μ shifts to higher energies and, at the extreme value of $x = 0.2$, the experimental density of carriers decreases by about 1 order of magnitude ($n_{300\,K} \approx 2 \times 10^{20}\,cm^{-3}$), consistent with the approach of μ to the band gap and the appearance of an experimental semiconductinglike regime [see resistivity in Fig. 6(a)] coming from the compensated holes. In the same rigid-band picture, we would expect μ at intermediate doping ($x = 0.1$) to fall in between the region defined by $x = 0$ and $x = 0.2$ [light blue area in Figs. 8(e)–8(g)]; however, this expectation contrasts with the experimental evidences of very large carrier density ($n_{300\,K} \approx 4 \times 10^{21}\,cm^{-3}$), lower (larger) resistivity, and slightly larger (slightly lower) carrier mobilities with respect to the $x = 0$ ($x = 0.2$) case. This discrepancy might point out limitations of the rigid-band approximation, which does not account for possible DOS differences arising from the formation of defects, as instead evidenced from our simulations. In this way, in the next sections, a possible defect-induced DOS feature is proposed to be responsible for the experimental observations.

VI. DISCUSSION

We first consider the effect of annealing. It is observed that annealing increases carrier mobility and slightly decreases hole carrier concentration. Moreover, relative heights of x-ray diffraction peaks I_{111}/I_{220} and I_{200}/I_{220} increase with annealing temperature, indicating increasing atomic order. Theoretical calculations indicate that hole carrier concentration is associated to atomic disorder, and carrier mobility is certainly limited by atomic disorder as well. Hence, all these

effects point to a healing effect of annealing on atomic disorder. Additionally, annealing is also found to improve homogeneity and phase purity.

We now turn to the effect of Sb substitution. The comparison of our transport results and *ab initio* calculations suggests that Sb substitution has a two-old effect: on one hand it fills bands with electron-type charge carriers, and on the other hand it is responsible for increased atomic disorder, which introduces hole-type charge carriers. The increased atomic disorder associated to Sb substitution is consistent with the progressive suppression of carrier mobility with increasing doping, even if the relative heights of x-ray diffraction peaks I_{111}/I_{220} and I_{200}/I_{220} do not exhibit any trend with increasing doping. In the 10%-doped sample, hole doping prevails, thus resulting in lower and metallic resistivity, monotonically increasing $S(T)$ dependence, and enhancement of the thermoelectric power factor at room temperature. In the 20%-doped sample, the level of introduced disorder is such that it yields much larger and semiconducting resistivity, decreased carrier density, $S(T)$ curve shape with a broad maximum at 200–250 K, and severe suppression of the thermoelectric power factor. Such effect of 20% doping could be explained in terms of disorder-induced Anderson localization [58]. As an alternative mechanism involving electric and thermoelectric data in Sb-doped samples, we suggest that increasing the Sb amount compensates part of the hole carriers whose presence is induced by native defects (antisites [49] and/or vacancies [17]) in the pristine Fe_2TiSn phase (see Fig. 8). In addition, the competition between the doped electrons and the defect-induced holes makes the system deviate from the monotonic behavior (expected in a rigid-band picture as a function of the doping level x) if we assume that the doping process shifts the chemical potential through a DOS peak, otherwise absent in the pristine structure, which lies close to the bottom of the valence band at intermediate Sb concentrations. This way, for $x = 0.1$, the number of carriers increases by 1 order of magnitude with respect to the undoped sample, although, due to the strongly localized nature of those defect states [see, for example, Figs. 8(a)–8(d)], the carrier mobility decreases and consequently the sample resistivity decreases only slightly. Hence, this scenario consistently explains the experimental behavior of resistivity, carrier density, mobility, and Seebeck coefficient, recovering at higher concentrations a semiconductinglike character as predicted for the pristine phase.

It is worth discussing the comparison between Fe_2TiSn and Fe_2VAl in terms of the role of doping in improving thermoelectric performances. The very large power factor predicted on Fe_2TiSn [11] is for strong n-type doping. Similar to Fe_2VAl [13], Fe_2TiSn forms as p-type doped and the atomic disorder affects significantly the electronic states near the band-gap edges. These states have significant contributions (orbital character) from Fe and V(Ti) atoms. From our knowledge, Fe_2TiSn has not been experimentally made as an n-type doped material, in contrast with Fe_2VAl [30–32,38]. This suggests that atomic site disorder in Fe_2TiSn plays a stronger role than in Fe_2VAl. For further insight into this comparison, we note that the findings of Chaudhuri *et al.* [49], that is, that the hole concentration increases with Sb doping and at the same time the concentration of antisite defects decreases with Sb doping, may be explained if the samples contain significant vacancy defects which act as p-type dopants and whose concentration increases with Sb doping. The presence of vacancy defects in Fe_2TiSn at a concentration significantly larger with respect to Fe_2VAl and the related Fermi-level pinning by the atomic defects (vacancies and antisite defects) may be the important differences between Fe_2TiSn and Fe_2VAl. Indeed, undoped Fe_2VAl has a dominant p-type transport character, with a high hole concentration of $\sim 4.8 \times 10^{20}$ cm^{-3} [59], while, from our data, undoped Fe_2TiSn forms as p-type doped with hole concentration $\sim 2 \times 10^{21}$ cm^{-3} at 300 K; the difference with Fe_2VAl is about 1 order of magnitude. A sizeable fraction of these holes may be associated to vacancies, whose concentration has been estimated up $\sim 10^{20}$ cm^{-3} in Fe_2TiSn samples grown by the optical floating zone technique [17]. In summary:

(1) In Fe_2TiSn the resonant and in-gap electronic states generated by vacancy and antisite defects (which are usually magnetic defects) can pin the Fermi level near the top of the valence band, making the n-type doping inefficient.

(2) The Anderson localization and hopping-type conduction, and magnetic(ferromagnetic) order may be stronger in Fe_2TiSn than in Fe_2VAl.

VII. CONCLUSIONS

We prepare polycrystalline Fe_2TiSn, $Fe_2TiSn_{0.9}Sb_{0.1}$, and $Fe_2TiSn_{0.8}Sb_{0.2}$ samples by arc melting in order to explore the possibility of improving thermoelectric power factor via Sb doping, as suggested by theoretical predictions. We find that the prepared samples present a sizeable amount of atomic disorder, which results in p-type transport and depressed thermoelectric properties. By comparison of experimental transport properties and *ab initio* calculations performed for atomic disorder, accounting for the existence of different antisite defects and vacancies, we sustain and demonstrate the origin of the measured p-type character of the transport in the undoped Fe_2TiSn, the origin of its magnetic ordering at low temperature, and, on the other hand, we provide an explanation for the observed reaction to Sb n-type doping, resulting in a compensated semiconductor. Specifically, in Sb-substituted samples annealed at 700 °C, we find that 10% substitution increases the hole carrier concentration, inducing a weakly metallic behavior, while 20% substitution lowers the carrier density and increases the resistivity by a factor ~50, restoring a semiconducting behavior, as in the undoped sample. We interpret this behavior in terms of competition between electron doping by band filling and hole doping associated to atomic disorder. In particular, to explain the nonmonotonic effect of Sb substitution on transport properties, we propose that the effectiveness of the doping process, acting in an already p-doped (and not pristine) crystalline environment, is affected by the DOS of the host material encountering its features induced by the presence of defects near the bottom of the valence band. Alternatively, we conjecture that in the 10% sample, the effect of defect-induced hole doping prevails over electron doping, while in the 20% sample, Anderson localization yielded by disorder eventually prevails on both electron and hole doping.

Focusing on the measured thermoelectric properties, the Seebeck coefficient exhibits a maximum at around 200–250 K for the semiconducting undoped and 20%-doped samples,

while it increases monotonically with temperature for the metallic 10%-doped sample. The temperature dependence of the Seebeck coefficient and the good electrical properties of the 10% sample determine the room-temperature power factor $\sim 1.3 \times 10^{-4}\,\mathrm{W\,K^{-2}\,m^{-1}}$ in this sample, more than twice as much as to the value of the undoped sample.

This experimental work indicates that improving the power factor by chemical doping is indeed possible in Fe_2TiSn (thermoelectric performances are indeed improved at low doping levels), yet the nature of real samples must be taken into account when designing possible substitutions. (The detrimental effect of atomic site disorder on electric and thermoelectric properties dominates at high doping levels, and this disorder should be minimized as much as possible.)

ACKNOWLEDGMENTS

F.R. and Ph.G. were supported by the European Funds for Regional Developments (FEDER) and the Walloon Region in the framework of the operational program "Wallonie-2020.EU" (project : Multifunctional thin films/LoCoTED). S.L. and Ph.G. were supported by the ARC project AIMED 15/19-09 785. Calculations have been performed on the Belgian Céci facilities funded by F.R.S-FNRS Belgium (Grant No. 2.5020.1) and Tier-1 supercomputer of the Fédération Wallonie-Bruxelles funded by the Walloon Region (Grant No. 1117545).

F.R. and S.L. contributed equally to the theoretical parts of the present manuscript.

[1] C. Chiritescu, D. G. Cahill, N. Nguyen, D. Johnson, A. Bodapati, P. Keblinski, and P. Zschack, Science **315**, 351 (2007).

[2] Z. Chen, X. Zhang, and Y. Pei, Adv. Mater. **30**, 1705617 (2018).

[3] J. He, M. G. Kanatzidis, and V. P. Dravid, Mater. Today **16**, 166 (2013).

[4] L.-D. Zhao, V. P. Dravid, and M. G. Kanatzidis, Energy Environ. Sci. **7**, 251 (2014).

[5] X. Shi, J. Yang, J. R. Salvador, M. Chi, J. Y. Cho, H. Wang, S. Bai, J. Yang, W. Zhang, and L. Chen, J. Am. Chem. Soc. **133**, 7837 (2011).

[6] H. Kleinke, Chem. Mater. **22**, 604 (2010).

[7] T. Zhu, C. Fu, H. Xie, Y. Liu, and X. Zhao, Adv. Energy Mater. **5**, 1500588 (2015).

[8] W. G. Zeier, J. Schmitt, G. Hautier, U. Aydemir, Z. M. Gibbs, C. Felser, and G. J. Snyder, Nat. Rev. Mater. **1**, 16032 (2016).

[9] T. Graf, C. Felser, and S. S. P. Parkin, Prog. Solid State Chem. **39**, 1 (2011).

[10] G. A. Slack, New materials and performance limits for thermoelectric cooling, in *CRC Handbook of Thermoelectrics*, edited by D. M. Rowe (CRC Press, Boca Raton, FL, 1995), pp. 407–440.

[11] D. I. Bilc, G. Hautier, D. Waroquiers, G.-M. Rignanese, and P. Ghosez, Phys. Rev. Lett. **114**, 136601 (2015).

[12] J. He, M. Amsler, Y. Xia, S. S. Naghavi, V. I. Hegde, S. Hao, S. Goedecker, V. Ozoliņš, and C. Wolverton, Phys. Rev. Lett. **117**, 046602 (2016).

[13] I. Knapp, B. Budinska, D. Milosavljevic, P. Heinrich, S. Khmelevskyi, R. Moser, R. Podloucky, P. Prenninger, and E. Bauer, Phys. Rev. B **96**, 045204 (2017).

[14] Y. G. Yu, X. Zhang, and A. Zunger, Phys. Rev. B **95**, 085201 (2017).

[15] V. Popescu, P. Kratzer, S. Wimmer, and H. Ebert, Phys. Rev. B **96**, 054443 (2017).

[16] M. L. C. Buffon, G. Laurita, L. Lamontagne, E. E. Levin, S. Mooraj, D. L. Lloyd, N. White, T. M. Pollock, and R. Seshadri, J. Phys.: Condens. Matter **29**, 405702 (2017).

[17] C. Hugenschmidt, A. Bauer, P. Böni, H. Ceeh, S. W. H. Eijt, T. Gigl, C. Pfleiderer, C. Piochacz, A. Neubauer, M. Reiner, H. Schut, and J. Weber, Appl. Phys. A **119**, 997 (2015).

[18] C. Uher, J. Yang, S. Hu, D. T. Morelli, and G. P. Meisner, Phys. Rev. B **59**, 8615 (1999).

[19] Y. Kimura, H. Ueno, and Y. Mishima, J. Electron. Mater. **38**, 934 (2009).

[20] W. Xie, Q. Jin, and X. Tang, J. Appl. Phys. **103**, 043711 (2008).

[21] M. Zhou, L. Chen, C. Feng, D. Wang, and J.-F. Li, J. Appl. Phys. **101**, 113714 (2007).

[22] M. Schwall and B. Balke, Appl. Phys. Lett. **98**, 042106 (2011).

[23] S. Sakurada and N. Shutoh, Appl. Phys. Lett. **86**, 082105 (2005).

[24] M. Schwall and B. Balke, Phys. Chem. Chem. Phys. **15**, 1868 (2013).

[25] C. Fu, T. Zhu, Y. Liu, H. Xiea, and X. Zhao, Energy Environ. Sci. **8**, 216 (2015).

[26] Y. Nishino, S. Deguchi, and U. Mizutani, Phys. Rev. B **74**, 115115 (2006).

[27] M. Mikami, Y. Kinemuchi, K. Ozaki, Y. Terazawa, and T. Takeuchi, J. Appl. Phys. **111**, 093710 (2012).

[28] K. Renard, A. Mori, Y. Yamada, S. Tanaka, H. Miyazaki, and Y. Nishino, J. Appl. Phys. **115**, 033707 (2014).

[29] T. Zou, T. Jia, W. Xie, Y. Zhang, M. Widenmeyer, X. Xiao, and A. Weidenkaff, Chem. Chem. Phys. **19**, 18273 (2017).

[30] H. Miyazaki, S. Tanaka, N. Ide, K. Soda, and Y. Nishino, Mater. Res. Express **1**, 015901 (2014).

[31] H. Matsuura, Y. Nishino, U. Mizutani, and S. Asano, J. Japan Inst. Metals **66**, 767 (2002).

[32] M. Vasundhara, V. Srinivas, and V. V. Rao, Phys. Rev. B **77**, 224415 (2008).

[33] G. D. Mahan and J. O. Sofo, Proc. Natl. Acad. Sci. USA **93**, 7436 (1996).

[34] S. Yabuuchi, M. Okamoto, A. Nishide, Y. Kurosaki, and J. Hayakawa, Appl. Phys. Express **6**, 025504 (2013).

[35] J. Rodriguez-Carvajal, Physica B **192**, 55 (1993), http://www.ill.eu/sites/fullprof/php/downloads.html.

[36] W. Kohn and L. J. Sham, Phys. Rev. **140**, A1133 (1965).

[37] R. Dovesi, R. Orlando, A. Erba, C. M. Zicovich-Wilson, B. Civalleri, S. Casassa, L. Maschio, M. Ferrabone, M. D. L. Pierre, P. D'Arco *et al.*, Int. J. Quantum Chem. **114**, 1287 (2014).

[38] R. Dovesi, V. R. Saunders, C. Roetti, R. Orlando, C. M. Zicovich-Wilson, F. Pascale, B. Civalleri, K. Doll, N. M. Harrison, and I. J. Bush *et al.*, CRYSTAL 14 User's Manual (2014).

[39] D. I. Bilc, R. Orlando, R. Shaltaf, G.-M. Rignanese, Jorge Íñiguez, and Ph. Ghosez, Phys. Rev. B **77**, 165107 (2008).

[40] I. P. R. Moreira, R. Dovesi, C. Roetti, V. R. Saunders, and R. Orlando, Phys. Rev. B **62**, 7816 (2000).

[41] T. Bredow, P. Heitjans, and M. Wilkening, Phys. Rev. B **70**, 115111 (2004).
[42] M. Towler, CRYSTAL resources page (2015), http://www.tcm.phy.cam.ac.uk/∼mdt26/.
[43] G. K. Madsen and D. J. Singh, Comput. Phys. Commun. **175**, 67 (2006).
[44] L. Romaka, V. V. Romaka, Yu. Stadnyk, and N. Melnychenko, Chem. Met. Alloys **6**, 12 (2013).
[45] M. Pani, I. Pallecchi, C. Bernini, N. Ardoino, and D. Marré, arXiv:1807.04545 [cond-mat.mtrl-sci].
[46] A. Slebarski, A. Wrona, T. Zawada, A. Jezierski, A. Zygmunt, K. Szot, S. Chiuzbaian, and M. Neumann, Phys. Rev. B **65**, 144430 (2002).
[47] C. S. Lue and Y.-K. Kuo, J. Appl. Phys. **96**, 2681 (2004).
[48] M. Nakabayashi, K. Fukuda, H. Kitagawa, Y. Yamada, S. Kubo, and A. Matsushita, Physica B **329-333**, 1134 (2003).
[49] S. Chaudhuri, P. A. Bhobe, and A. K. Nigam, J. Phys.: Condens. Matter **30**, 015703 (2018).
[50] A. Slebarski, M. B. Maple, E. J. Freeman, C. Sirvent, D. Tworuszka, M. Orzechowska, A. Wrona, A. Jezierski, S. Chiuzbaian, and M. Neumann, Phys. Rev. B **62**, 3296 (2000).
[51] A. Slebarski, J. Phys. D: Appl. Phys. **39**, 856 (2006).
[52] H. Luo, G. Liu, F. Meng, J. Li, E. Liu, and G. Wu, J. Magn. Magn. Mater. **324**, 3295 (2012).
[53] B. Abeles, Phys. Rev. **131**, 1906 (1963).
[54] J. Callaway, Phys. Rev. **113**, 1046 (1959).
[55] J. C. Slater, Phys. Rev. **49**, 931 (1936).
[56] L. Pauling, Phys. Rev. **54**, 899 (1938).
[57] D. I. Bilc and P. Ghosez, Phys. Rev. B **83**, 205204 (2011).
[58] P. W. Anderson, Phys. Rev. **109**, 1492 (1958).
[59] M. Kato, M. Kato, Y. Nishino, U. Mizutani, and S. Asano, J. Jpn. Inst. Met. **62**, 669 (1998).